

Wavelength-dependent PSFs and their impact on weak lensing measurements

S. G. Carlsten,¹★ Michael A. Strauss,¹ Robert H. Lupton,¹ Joshua E. Meyers^{1,2} and Satoshi Miyazaki^{3,4}

¹*Department of Astrophysical Sciences, 4 Ivy Lane, Princeton University, Princeton, NJ 08544, USA*

²*Kavli Institute for Particle Astrophysics and Cosmology, Department of Physics, Stanford University, Stanford, CA 94305, USA*

³*National Astronomical Observatory of Japan, 2-21-1 Osawa, Mitaka, Tokyo 181-8588, Japan*

⁴*Department of Astronomical Science, SOKENDAI (The Graduate University for Advanced Studies), 2-21-1 Osawa, Mitaka, Tokyo 181-8588, Japan*

Accepted 2018 June 19. Received 2018 June 18; in original form 2018 April 11

ABSTRACT

We measure and model the wavelength dependence of the point spread function (PSF) in the Hyper Suprime-Cam Subaru Strategic Program survey. We find that PSF chromaticity is present in the redder stars that appear smaller than bluer stars in the g , r , and i bands at the 1–2 per cent level and in the z and y bands at the 0.1–0.2 per cent level. From the color dependence of the PSF, we fit a model between the monochromatic PSF size based on weighted second moments, R , and wavelength of the form $R(\lambda) \propto \lambda^{-b}$. We find values of b between 0.2 and 0.5, depending on the epoch and filter. This is consistent with the expectations of a turbulent atmosphere with an outer scale length of $\sim 10 - 100$ m, indicating that the atmosphere is dominating the chromaticity. In the best seeing data, we find that the optical system and detector also contribute some wavelength dependence. Meyers & Burchat showed that b must be measured to an accuracy of ~ 0.02 not to dominate the systematic error budget of the Large Synoptic Survey Telescope (LSST) weak lensing (WL) survey. Using simple image simulations, we find that b can be inferred with this accuracy in the r and i -bands for all positions in the LSST focal plane, assuming a stellar density of 1 star arcmin⁻² and that the optical component of the PSF can be accurately modeled. Therefore, it is possible to correct for most, if not all, of the bias that the wavelength-dependent PSF will introduce into an LSST-like WL survey.

Key words: gravitational lensing: weak – atmospheric effects – instrumentation: detectors – methods: observational.

1 INTRODUCTION

To make use of the statistical power of upcoming wide-field imaging surveys, systematic biases in cosmological weak lensing (WL) measurements need to be very well constrained. One such effect is the chromaticity of the point spread function (PSF), in the sense that the PSF changes in size and shape as a function of wavelength across a given broad-band. Since the stars from which the PSF is typically measured have different spectral energy distributions (SEDs) from the galaxies that the cosmic shear is measured from, there is error in applying the stellar PSF to the galaxies when using broad-band data. Stellar and galactic PSFs can differ in size at the 1 per cent level for certain conditions, which is well above the systematic error budgets for upcoming WL imaging surveys (e.g. Massey et al. 2013). Huterer et al. (2006) and Amara & Réfrégier

(2008) estimate that for a WL survey with the coverage of the Large Synoptic Survey Telescope (LSST; LSST Science Collaboration et al. 2009), the average, uncorrected multiplicative bias to the shear needs to be $\lesssim 0.003$ for the uncertainty in the estimates of cosmological parameters to be degraded by less than $\sqrt{2}$ times the purely statistical uncertainty. This corresponds to requiring that the systematic error in the PSF model size be constrained to < 0.1 per cent (Paulin-Henriksson et al. 2008).

Cypriano et al. (2010) first discussed the issue of PSF chromaticity and explored how the effective PSF for a galaxy was different from that for a star in a diffraction-limited telescope. Meyers & Burchat (2015b) extended this work, using a more realistic model for the chromaticity of the PSF for ground-based surveys. They use the standard Kolmogorov turbulent atmosphere result that the seeing scales as $\lambda^{-0.2}$ (Roddier 1981). They find that the bias caused by using a stellar PSF can be corrected for at roughly the level of the LSST systematic error budget by correcting the PSFs on an

★ E-mail: scottgc@princeton.edu

‘object-by-object’ basis using multiband photometry of each object and comparing with a large library of galactic SEDs. Eriksen & Hoekstra (2018) do a similar investigation assuming the filters of the *Euclid* space-based survey (Laureijs et al. 2011) and an optical model of *Euclid* in which the size of the PSF $\propto \lambda^{0.55}$. Voigt et al. (2012) and Semboloni et al. (2013) consider how a wavelength-dependent PSF will couple with a galaxy’s colour gradient to bias the measurement of shape. Alejandro Plazas & Bernstein (2012) and Meyers & Burchat (2015b) also discuss how differential chromatic refraction can bias shear measurements from the LSST by introducing an SED-dependent elongation of the PSF along the elevation vector.

The previous works all assume an *a priori* model for the PSF as a function of wavelength. In this paper, we extend these previous studies by measuring the chromaticity of the PSF from ground-based data from the Hyper Suprime-Cam (HSC) survey. This can be done from stars of different colour in the image frames. This is most important for ground-based surveys in which the atmosphere, optics, and detector together create the wavelength dependence, making this dependence nearly impossible to know *a priori*.

The main concern is that the chromaticity due to the atmosphere will vary from night to night and possibly even within a night. The Kolmogorov atmosphere theory assumes a scale-free spectrum of turbulence but overpredicts the observed turbulence at larger scales (Coulman et al. 1988; Conan et al. 2000; Ziad et al. 2000; Linfield, Colavita & Lane 2001; Tokovinin, Sarazin & Smette 2007). The ‘von Kármán’ turbulence model (von Kármán 1948) imposes an outer scale beyond which the wavefront structure function flattens; this model is a better fit to observational data (e.g. McKechnie 2016; Oya et al. 2016), as we demonstrate in this paper. The von Kármán model is found to adequately fit the PSFs present in the Sloan Digital Sky Survey imaging (Xin et al. 2018). The outer scale can vary from ~ 10 to 100 m for common observatory sites (e.g. Conan et al. 2000; Ono et al. 2017) and will change from day to day and even within a night (Linfield et al. 2001). This outer scale effectively steepens the chromaticity of the PSF over the Kolmogorov case (Tokovinin 2002; Martinez et al. 2010). In Appendix A, we show this, and review atmospheric turbulence theory as it applies to observed PSFs.

In addition to the atmosphere, there is the possibility of chromaticity from the telescope and instrument, either from the optical design or construction or alignment errors. Diffraction-limited optics will have PSF size $\propto \lambda$. The charge diffusion present in CCDs will also contribute some chromaticity (Meyers & Burchat 2015a) due to the wavelength dependence of the photon absorption length in silicon. The relative contributions of the atmospheric chromaticity and that of the optics/detector will depend on the seeing, which is a function of time.

In WL, both the ellipticity and overall size of the PSF need to be accurately modelled. Mis-modelling the PSF size will directly lead to a multiplicative bias in the shear. Mis-modelling the PSF ellipticity can result in an additive bias whose amplitude depends on the spatial correlations of the ellipticity errors (for a recent review of WL systematics, see Mandelbaum 2017). In this paper, we consider only the simpler case of modelling the wavelength dependence of the PSF size.

There are other PSF effects that also need to be corrected for at this level of precision, including the brighter-fatter effect and variations of the PSF across the focal plane due to detector non-uniformities, optics, and atmospheric turbulence. The brighter-fatter effect comes from the lateral electric field generated from charge build-up in the pixel wells of the detector (Antilogus et al. 2014) and can be modelled by considering the correlations between pixels

in flat-field images (Coulton et al. 2017). Spatial variations in the PSF are usually modelled as a low-degree polynomial function of position on a chip (e.g. Lupton et al. 2001; Jee & Tyson 2011) for each chip on the focal plane. Since the colours of stars should be independent of position on the sky, this effect is separable from the chromatic effect we investigate here.

In Section 2, we analyse and discuss the chromaticity present in data from the Hyper Suprime-Cam Strategic Survey Program (HSC SSP). In Section 3, we use simulations to address how well the chromaticity can be measured for various survey parameters. In Section 4, we discuss our results and conclude.

2 HSC DATA

The HSC SSP survey is an ongoing optical imaging survey in five broad-bands (*grizy*) (Aihara et al. 2018a) with the Hyper-Suprime Camera (Furusawa et al. 2018; Komiyama et al. 2018; Miyazaki et al. 2018; Kawanomoto et al. in prep) on the 8.2-m Subaru telescope operated by the National Astronomical Observatory of Japan. Because of its coverage, depth, and image quality (0.6 arcsec median seeing in *i* band) the survey acts as a test bed and precursor for the upcoming LSST (LSST Science Collaboration et al. 2009). In brief, the HSC instrument includes a wide-field corrector (WFC) that has an atmospheric dispersion corrector and delivers images with <0.2 arcsec full width at half-maximum (FWHM; instrumental contribution only) across a $1^\circ 5$ diameter field of view. The focal plane is paved with $104\ 2k \times 4k$ science CCDs over $1.7\ \text{deg}^2$. The CCDs are $200\ \mu\text{m}$ thick Hamamatsu devices with $15\ \mu\text{m}$ wide pixels (Miyazaki et al. 2018) subtending 0.168 arcsec. The survey consists of three layers with different sky coverages and depth: the wide layer will cover $1400\ \text{deg}^2$ and go to ~ 26 mag in *r*, the deep layer will cover $26\ \text{deg}^2$ and go to ~ 27 mag in *r*, and the ultra-deep layer will cover $3.5\ \text{deg}^2$ and go to ~ 28 mag in *r*. The first data release of the survey, consisting of data taken in 2014 and 2015, has been released to the public¹ (Aihara et al. 2018b). Details of the HSC data reduction pipeline can be found in Bosch et al. (2018). The pipeline makes use of much of the software being developed for the LSST (Ivezić et al. 2008; Axelrod et al. 2010; Jurić et al. 2015).

2.1 Data Selection

To investigate the level of chromaticity present in the HSC survey data, we measure the PSF size as a function of colour. To this end, we use single epoch, single band exposures (called ‘visits’ in the pipeline). Roughly 500 visits in each of the bands are randomly selected from the S15B internal data release, which includes data taken over many nights in 2014 and 2015 from the wide, deep, and ultra-deep layers. The visits from the ultra-deep, deep, and about 1/3 of the wide-layer visits are included in the 2017 public data release (Aihara et al. 2018b). Exposure times for individual visits in the wide layer are 150 s for the *g* and *r* bands and 200 s for the *i*, *z*, and *y* bands. Exposure times for the deep layer are 180 s for the *g* and *r* bands and 270 s for the *i*, *z*, and *y* bands. All bands have 300 s exposure times in the ultra-deep layer visits. Visits from each of the three layers are treated here identically. The seeing in the visits ranges from ~ 0.5 to ~ 1.2 arcsec. The HSC pipeline (Bosch et al. 2018) identifies candidate stars for PSF modelling using a *k*-means clustering algorithm on the size of detected sources. Candidates

¹The data release website is <https://hsc-release.mtk.nao.ac.jp/>

are further restricted to sources brighter than 12 500 counts (~ 22.3 mag in i in the wide layer). For this analysis, we just consider these candidate stars for PSF modelling.

In the pipeline, the multiple visits in each band covering a given area are warped to a common pixel grid and coadded together. Object detection is run on this coadd and a catalogue for the coadd is made. To get colours for each source, we cross-reference the single-visit catalogue with the coadd catalogue for that area. We expect that the PSF size in a band will depend on the slope of the source's SED across that band, therefore we use the colour for each band that most closely represents that slope. For g -band visits we consider the $g - r$ colour, for r -band we use the $g - i$ colour, for i -band visits we consider the $r - z$ colour, for z -band visits we consider the $i - y$ colour, and, finally, for y -band visits we consider the $z - y$ colour. Using the simulations described in Section 3, we determined that these colours used for the r , i , and z bands were slightly better at constraining the wavelength dependence of the PSF than colours that include the band of the visit being processed. This is due to a somewhat larger dynamic range in usable colours with the longer baseline and the fact that shape and photometric measurements will be uncorrelated when using the colours with the longer baseline.

As described below, we infer the wavelength dependence using a library of stellar SEDs. Since this library does not account for unresolved binaries, quasars, or other classes of contaminating point sources, we restrict to sources located on the stellar colour–colour loci. For g - and r -band visits, we consider the $g - r$ versus $r - i$ locus. For i -band visits, we consider the $r - i$ versus $i - z$ locus. For z - and y -band visits, we consider the $i - z$ versus $z - y$ locus. We restrict the single-visit catalogue to sources that appear in all three coadd catalogues that make up the appropriate colour–colour diagram. As described below, further colour cuts are imposed so that the PSF size–colour relation is accurately linear. Over these colour ranges, the colour–colour loci are also roughly linear and we fit lines to the loci and only take sources within 0.08 dex of the locus. This is roughly twice the natural thickness of the $g - r$ versus $r - i$ locus from Covey et al. (2007). All these cuts leave us with approximately 2000–8000 sources for each visit. Considering the 1.7 deg^2 field of view of HSC, this is approximately 1 source arcmin^{-2} .

The pipeline corrects for the brighter-fatter effect by using the pixel covariances found in flat-fields to reapportion the flux, as described in Coulton et al. (2017). The HSC pipeline then models the PSF with the PSFEX (Bertin 2013) software. The PSF is modelled on a pixel basis and spatial variations of the PSF in a given visit are captured with a third degree polynomial function of the position on a chip. Sources of all colour are used in the PSF modelling and so chromatic effects are not accounted for. The pipeline quantifies the size of a source with its ‘trace radius’ defined as

$$R \equiv \sqrt{I_{xx} + I_{yy}}, \quad (1)$$

where I_{xx} and I_{yy} are the two second moments. The second moments are measured with the Hirata-Seljak-Mandelbaum (HSM) adaptive weighting scheme of Hirata & Seljak (2003) as implemented in GALSIM (Rowe et al. 2015).² We use this definition for the PSF size throughout since it is directly relatable to the multiplicative bias

²The calculated second moments are Gaussian weighted, so they deviate slightly from true second moments because the PSF is not described by a Gaussian. Nevertheless, these second moments are a robust measure of source size.

in the shear caused by PSF mis-modelling (e.g. Paulin-Henriksson et al. 2008). For a Gaussian PSF, the FWHM is ~ 1.665 times the trace radius. For a characteristic HSC PSF, the ratio is closer to 1.5 due to the large non-Gaussian wings.

The HSC pipeline provides size estimates of both the source and the PSF model at the location of the source. We use the PSF model to ‘correct’ for the spatial variation of the PSF by subtracting the PSF model size, R_{PSF} , from the measured source size in quadrature for each PSF candidate star and then adding the median PSF model size, $\langle R_{\text{PSF}} \rangle$, for the visit, using the full 1.5 wide FOV, also in quadrature. Thus, the corrected PSF size is

$$R_{\text{corr}}^2 = R_{\text{meas}}^2 - R_{\text{PSF}}^2 + \langle R_{\text{PSF}}^2 \rangle. \quad (2)$$

This should account for the spatial variations of the PSF without affecting the chromatic variations, since those will appear in the residuals of the PSF model.

As shown in Mandelbaum et al. (2018), the pipeline PSF modelling is quite good, with modelling errors less than 2 per cent of the PSF size for almost all sources selected as PSF model candidate stars. The median PSF size error in the first year data is found to be < 0.4 per cent in the i band, which is within the requirements for first year WL science. Fig. 1 shows source size versus source colour for one visit in each of the g , r , i , and z bands. The g , r , and i band PSFs show a reasonably strong trend with colour (~ 1 per cent across the colour range), whereby redder sources are smaller. The z and y bands (the latter not shown) do not show a strong trend, for reasons that will be discussed below.

2.2 Model Fits

As stated in the introduction, if one can model the monochromatic PSF as a function of wavelength, then the chromatic bias in a WL survey can be removed by calculating ‘per-object’ PSFs for objects with arbitrary SEDs. Therefore, we wish to infer the monochromatic PSF size versus wavelength relations from the observed dependence of the broad-band PSF size versus colour. The observed PSF image in a band is the average of the monochromatic PSF weighted by the source SED. To infer a monochromatic size versus wavelength model from an observed size versus colour relation for stellar sources, we need a library of stellar SEDs. We use the library of the LSST Catalog Simulator³ (CATSIM) (Connolly et al. 2014), which is used in the LSST Photon Simulator (PHOSIM) (Peterson et al. 2015). The SEDs are synthetic and use the Kurucz (1993) library down to an effective temperature of 4000 K, and the low-mass models of Baraffe et al. (2015) for cooler stars. The models include a range in metallicities from $[\text{Fe}/\text{H}] = -4$ to $[\text{Fe}/\text{H}] = 1$ for the Kurucz models, and range from $[\text{Fe}/\text{H}] = -4$ to $[\text{Fe}/\text{H}] = 0.5$ for the low-mass models.

Since the relative populations of different types of stars (the number of high-mass versus low-mass stars, for instance) will influence our fits, we use the simulated universe of the LSST CATSIM project to generate a realistic sample of SEDs. The Milky Way stellar population in CATSIM uses the GALFEST model of M. Jurić, which is based on star counts using the Sloan Digital Sky Survey (SDSS) (Jurić et al. 2008; Ivezić et al. 2008) and has a realistic stellar colour distribution. Samples of stars with $18 < i < 23$ are generated in 0.1 radii circles at 10 random locations in the HSC survey footprint. This magnitude range roughly corresponds to the magnitude range of stars selected from the data. We use the combined catalogue of

³<https://www.lsst.org/scientists/simulations/catsim>

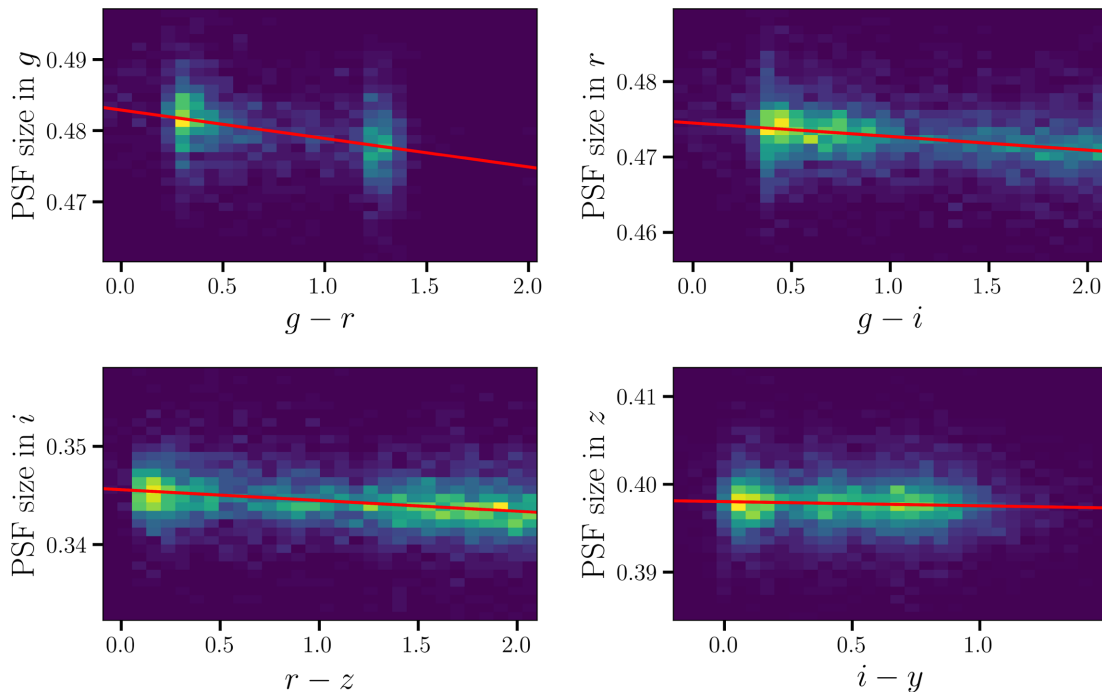


Figure 1. 2D histograms showing the source size (in arcseconds) versus colour for stellar sources in one ($\sim 1.7\text{deg}^2$) HSC visit in each of the four bands *griz*. Here the PSF size, R , is quantified as trace radius measured from the weighted second moments of the image of each star. The FWHM of the PSF is roughly $\sim 1.5R$. The source size has been corrected for the spatial variation of the PSF across the HSC field of view (equation 2). The red line is a linear fit to the data, highlighting the downward trend in the *g*, *r*, and *i* bands. The bimodal distribution of stars in *g-r* is astrophysical and can be seen, for example, in the SDSS colour–colour diagrams of Covey et al. (2007).

model stellar SEDs of these samples in what follows. We find no significant difference in the following analysis if a different set of 10 locations are used or if the empirical Pickles library (Pickles 1998) is used instead.

We denote the monochromatic PSF size as a function of wavelength as $R(\lambda)$, and assume that it varies with wavelength in the form of a power law:

$$R(\lambda) \propto \left(\frac{\lambda}{5000\text{\AA}} \right)^{-b}. \quad (3)$$

We denote the broad-band PSF size as a function of colour as $R(c)$ (as in Fig. 1). The observed PSF size of a star with SED F and colour c in a band is⁴

$$R^2(c) = \frac{\int d\lambda G(\lambda) F(\lambda, c) R^2(\lambda)}{\int d\lambda G(\lambda) F(\lambda, c)}, \quad (4)$$

where $G(\lambda)$ is the instrument’s response in the band. Fig. 2 plots the PSF size from equation (4) as a function of colour for each SED in the library, assuming $R(\lambda) \propto \lambda^{-0.35}$ (which we find below is a reasonable model). Because there is close to a one-to-one correspondence between stellar colour and SED, the PSF size is mostly just a function of the SED’s colour.

Nonetheless, to reduce the scatter seen in the SED library in Fig. 2 at the red edge, we consider only the restricted colour intervals over which the PSF size–colour relation is accurately linear and single-valued: $g-r \in [0, 1.0]$ for g , $g-i \in [0, 1.8]$ for r , $r-z \in [0, 2.0]$ for i , $i-y \in [-0.2, 0.7]$ for z , and $z-y \in [-0.1, 0.5]$ for y . These

restricted ranges will make the analysis less sensitive to the relative populations of stars in the SED library.

We generate plots like Fig. 2 for several values of b in equation (3) and measure the slope in each case. The slopes are normalized by the y-intercept of the line (i.e. at colour of 0) to account for different normalizations of the PSF size (caused by different levels of seeing). This gives us a lookup table between the PSF size–colour slope and the power-law exponent, b , in the PSF size–wavelength relation; the two quantities are almost linearly related.

This now gives us a way to infer the value b for a given visit in a given band. We fit lines to the observed PSF size–colour relation in each visit and in each band, as in Fig. 1. The slope of the PSF size–colour relation is normalized by the y-intercept of the fitted line, and the index b is inferred from the lookup table. The size–colour relation is fit with a standard least squares minimization giving all sources equal weight, with two iterations of 3σ clipping. Since there are unknown uncertainties from PSF modelling errors in addition to measurement uncertainties of the second moments, we cannot derive meaningful error bars from the fits directly. Instead, in Section 3 we address how accurately the wavelength dependence (i.e. the parameter b) can be determined using detailed simulations.

In Fig. 3, we plot the inferred power-law exponent, b , as a function of the seeing in each of the visits processed. To determine the seeing, the FWHM (not trace radius) is measured from the PSF model averaged over all of the chips for a particular visit. It is seen that the power-law exponent varies quite a bit between visits but is mostly in the range 0.0–0.5. The different bands show different trends with the seeing. In the *g* and *r* bands, there is a slight drop in the power-law exponent at very good seeing. In the *i* and *y* bands, there does not seem to be any trend. Finally, in the *z* band, there is a noticeable increase in b for good seeing. We will explore these trends in the

⁴This expression ignores the fact that we use weighted second moments to measure $R(c)$, but the error due to this approximation is only ~ 1 per cent in the inferred wavelength dependence of the PSF.

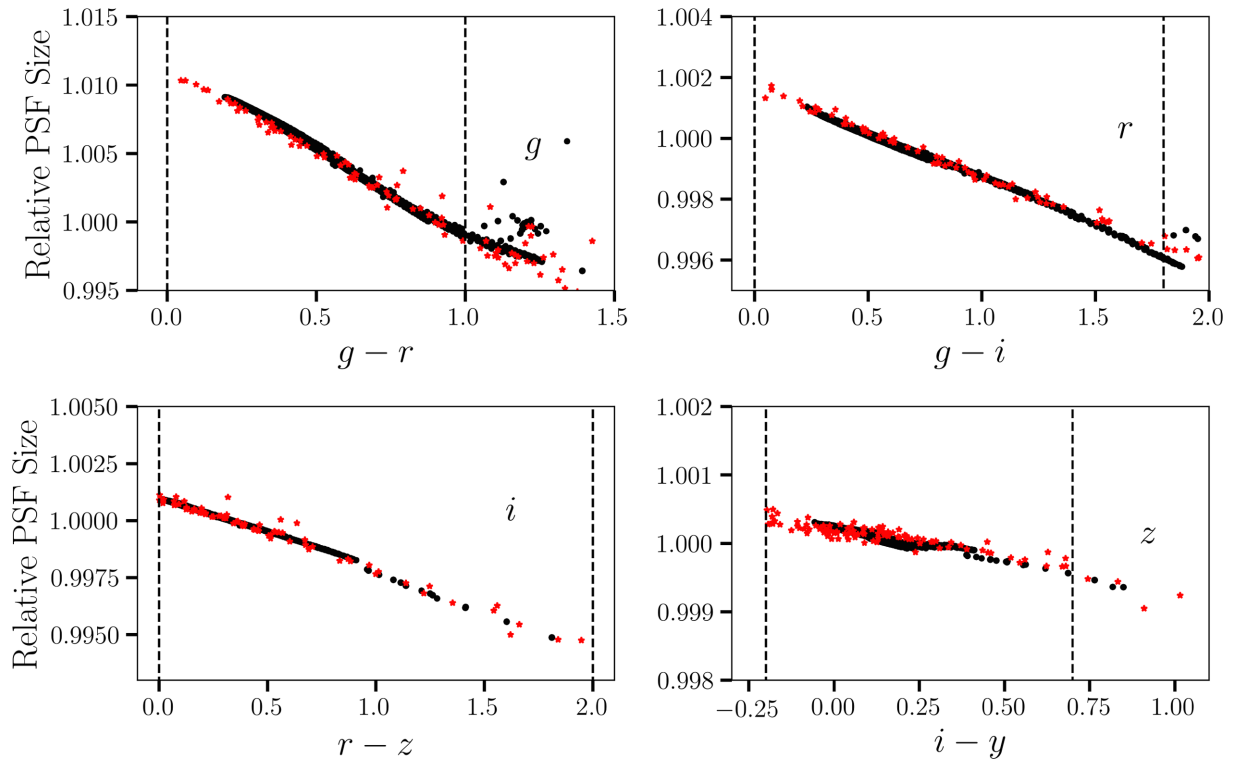


Figure 2. Predicted PSF size (cf. equation 4) relative to the median in the *griz* bands versus colour using the library of stellar SEDs described in the text. Black points are the synthetic library and red stars show the Pickles library. The monochromatic PSF size is assumed to scale with wavelength as $R(\lambda) \propto \lambda^{-0.35}$. For the most part, the PSF size depends only on the colour of the SED, and the slopes of the relation are the same in the two SED libraries. The dashed lines show the imposed colour cuts to ensure the PSF size–colour relation is accurately linear.

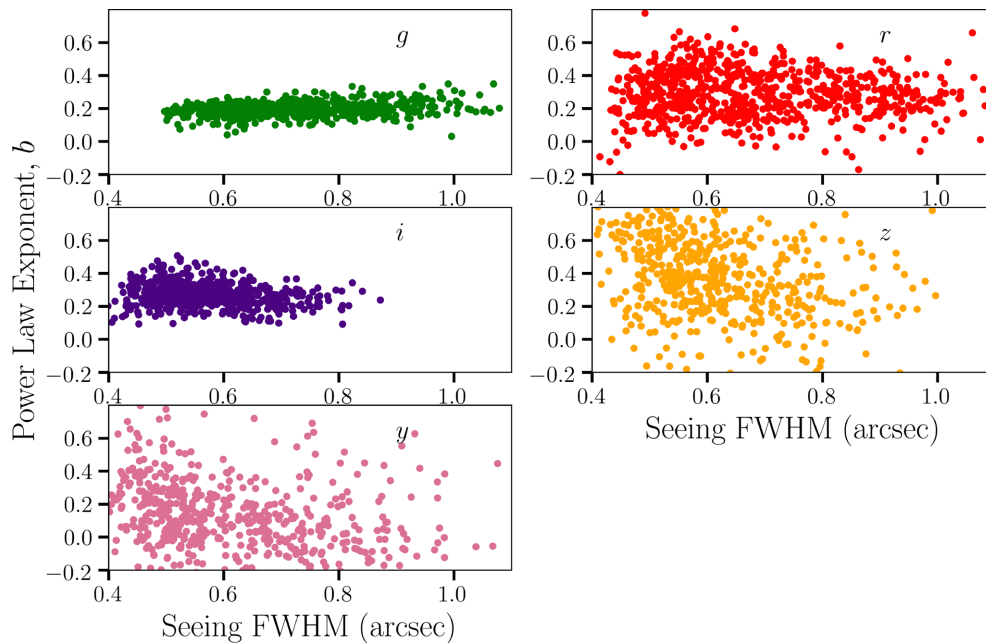


Figure 3. The (negative) power-law exponent of equation 3, i.e. the parameter b , as a function of the seeing in each visit. Each panel is a different band, as indicated in the corner of each subplot. Note that the *i*-band data have significantly better median seeing than the other bands (Aihara et al. 2018a).

next section in light of a simplified model of the optical/instrumental PSF.

The scatter in the points also depends on the band, being significantly greater for the *r*, *z*, and *y* bands. There are several reasons for

this: the colour cut in *r* significantly reduces the number of sources used, the *z*-filter is narrower than the other filters, there is more variation in atmospheric absorption in the *z* and *y* bands, and stellar SEDs all have similar slopes through the *z* and *y* bands that lead to

Table 1. Median power-law exponents, b , for all visits for sources within the inner 0:3, and the outer 0:2 of the field of view, respectively, of HSC. The error is the standard error in the mean of the visits. The smaller number of sources in the y band made many of the fits unstable, so it was not considered here.

Band	Inner 0:3	Outer 0:2
g	0.208 ± 0.003	0.198 ± 0.003
r	0.319 ± 0.008	0.278 ± 0.005
i	0.259 ± 0.004	0.268 ± 0.003
z	0.388 ± 0.030	0.381 ± 0.015

a smaller difference in size between blue and red sources, making it difficult to measure the slope. While the PSF size of red and blue sources may differ by 1 per cent or more in the g , r , and i bands, the difference is only of the order of 0.1 per cent in the z and y bands (Figs 1 and 2). In fact, many of the y -band visits in Fig. 3 appear consistent with a power-law exponent of 0 (i.e. no chromatic dependence). Note that the range in seeing is much smaller in the i band than the other four bands, due to the HSC observing survey strategy (Aihara et al. 2018a); the i -band data are only taken in <0.8 arcsec seeing.

The level of chromaticity depends only very weakly on position in the focal plane. Considering either only sources in the inner 0:3 radius or the outer 0:2 of the field of view yields mildly different average power-law exponent only for the r band (Table 1); the difference is insignificant in g , i , and z . For r band, the chromaticity is less steep in the outer regions.

2.3 HSC Optical Model

When the atmospheric seeing is very good, the instrumental contribution to the PSF will become more significant. In this section, we quantify this contribution in the context of the different behaviour of the chromaticity as a function of seeing in different bands (cf. Fig. 3). We will consider two sources of the instrumental contribution to the PSF: the image size produced by the WFC and charge diffusion in the CCD detectors. The WFC gives an achromatic, but large, contribution to the instrumental PSF and thus dilutes other sources of chromaticity. Charge diffusion refers to the lateral spreading of the electrons as they move through the silicon layer. The amount of spreading depends on the distance traversed through the silicon. The expected diffusion has an rms spread of around $7 \mu\text{m}$, given the $200 \mu\text{m}$ thickness of the HSC CCDs (Miyazaki et al. 2018). This spread is assumed to be independent of the brightness of a source (i.e. the brighter-fatter effect has already been corrected for as described above). Note that the HSC pixels are $15 \mu\text{m}$ wide with pixel scale 0.17 arcsec per pixel so the diffusion is a small effect. Charge diffusion is a function of wavelength because photons of wavelength longer than 700 nm penetrate a significant depth into the silicon before converting to an electron-hole pair. This leaves the electron with less remaining silicon to traverse, decreasing the charge diffusion. The amount of charge diffusion is smaller if the CCDs are run with a higher bias voltage but we assume that this does not change between visits. Miyazaki et al. (2018) performed tests on the constructed HSC system and provide estimates of the contribution of the WFC and charge diffusion to the optical PSF. In Tables 2 and 3, we reproduce their tables 4 and 9 describing the image-size specifications of the WFC and amount of charge diffusion, respectively. For a Gaussian PSF, the 80 per cent encircled energy diameter of Table 2 is 1.5 times the FWHM.

Table 2. Table 4 from Miyazaki et al. (2018). Image size delivered by the WFC, not including the contribution from the atmosphere. Estimated sizes are given as D_{80} , the diameter enclosing 80 per cent of image flux. Sizes for telescope elevation of 90° and 30° are included.

Band	Central λ (\AA)	$EL=90^\circ$ (arcsec)	$EL=30^\circ$ (arcsec)
g	4700	0.199	0.234
r	6200	0.197	0.232
i	7600	0.200	0.233
z	9100	0.206	0.214
y	10200	0.210	0.228

Table 3. Table 9 from Miyazaki et al. (2018). Image size due to charge diffusion in the CCDs.

λ (nm)	rms spread (μm)	FWHM (arcsec)
700	6.9	0.18
800	6.6	0.17
900	5.8	0.15
1000	4.5	0.12

It is worth noting that the wavelength-dependent absorption length of photons in silicon can lead to another, opposite chromatic effect. Because the HSC beam is fast ($f/2$), photons will be incident onto the silicon at a fairly steep angle. Since redder photons will be absorbed over a wider range of depth in the silicon, the lateral spread of photons in the incident beam can lead to a larger image size for longer wavelengths. This effect is essentially due to the fact that red photons will not all be absorbed at the depth of best focus within the silicon. Meyers & Burchat (2015a) argue that for the LSST this effect will dominate over the charge diffusion effect described above due to the extremely fast $f/1.2$ LSST beam. For HSC however, Miyazaki et al. (2018) estimate that this effect's contribution to the total instrumental PSF is roughly a factor of 3 less than that from charge diffusion, at least at the telescope boresight. It is unclear whether this is still the case near the edge of the field of view where the incident angle of the photons will be steeper, but here we assume that it is and ignore this additional chromatic effect.

Adding the values in Tables 2 and 3 in quadrature, the final instrumental PSF widths used are shown in Fig. 4. We use image sizes for the WFC at a telescope elevation of 30° . While this is conservative, we are not including other contributors to the PSF, such as tracking errors and wind jitter. To measure the slope of the PSF size across the whole y band, we add another data point at 10500 \AA , extrapolated from the trend from z to y . The nearly complete transparency of silicon to photons of this wavelength is expected to cause a significant increase in PSF size on the redward edge of y , as explained below. The final value we choose (see Fig. 4) is somewhat arbitrary.

We can combine the instrumental PSF estimate along with predictions for a turbulent atmosphere to understand the trends seen in Fig. 3. To do this, we generate atmospheric PSFs using the von Kármán model with a given outer scalelength and with different levels of seeing as discussed in Appendix A and then convolve this PSF with a Gaussian representing the optical/instrumental components combined together in quadrature.⁵ Monochromatic PSFs for several different wavelengths are generated in each band for a range

⁵A Gaussian accurately represents charge diffusion's contribution to the PSF, while the optical component will have more high frequency power. For this analysis, however, a Gaussian is likely to be an adequate approximation.

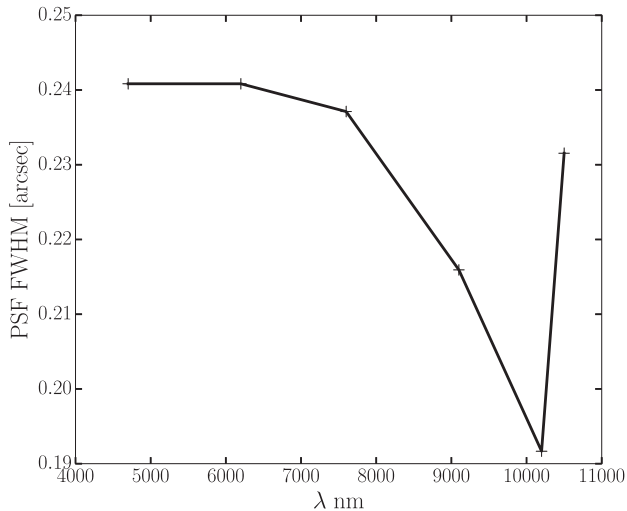


Figure 4. The assumed width of the instrumental component of the PSF at different wavelengths, assuming a telescope elevation of 30° . The spike at $10\,500\text{ \AA}$ represents the assumed increase in PSF size at the redward edge of the y band (see the text).

of seeing values. The trace radii of these PSFs are measured and a power law is fit as a function of wavelength. We then plot the expected power-law exponent versus the average FWHM seeing in that band.

Fig. 5 shows the data of Fig. 3 smoothed with a running mean, along with the expectations for an atmospheric outer scalelength of 8 m, 25 m, and the Kolmogorov result with no outer scale, all convolved with the instrumental PSF of Fig. 4. 25 m is the characteristic outer scalelength for many observatory sites, including Maunakea (Ziad et al. 2000; Ono et al. 2017). With the exception of y band, the models seem to predict, at least qualitatively, the behaviour in the different bands. The models predict a drop in the power-law exponent at good seeing that is visible in the data in the g and somewhat in the r band at the very good seeing edge. The instrumental PSF shows less chromaticity than the atmospheric PSF in these bands, so the level of chromaticity drops (smaller b) as the seeing gets better.

The opposite situation occurs in the z band where the level of charge diffusion depends steeply on wavelength, as shown in Table 3. Here, the instrumental PSF has a steeper wavelength dependence than the atmospheric PSF, leading to increased power-law exponent at better seeing. The same situation should be true in the y band, but the increased transparency of the silicon to photons on the redward edge of y is so great that these photons actually bounce off the bottom of the silicon and get absorbed on the way back to the top surface. These photons get diffracted off the gate pattern on the bottom of the silicon, leading to a large cross-shaped pattern containing roughly 2 per cent of the flux around stars in HSC y images (Gunn, private communication). An example of this pattern is shown in Fig. 6. This leads to a larger instrumental PSF on the red edge of y , as we have assumed in our model (cf. Fig. 4). The diffracted light increases the measured PSF trace radius in y by 0.1–0.2 per cent, roughly cancelling out the chromatic effect of the atmosphere and leading to little net chromaticity in this band.

We can now understand the spatial variation of the wavelength dependence shown in Table 1. Fig. 4 of Miyazaki et al. (2018) shows the designed performance of the WFC as a function of position in the focal plane. r band shows the most significant increase in image size between the inner $0:3$ and outer $0:2$ regions. Since the

instrumental component of the PSF in the r band is essentially wavelength independent, the overall chromaticity decreases in the outer region of the focal plane as the instrumental PSF dilutes the chromaticity from the atmosphere, which is what we observe.

3 SIMULATIONS

In the previous section, we showed that the PSF is significantly chromatic in the HSC-SSP survey. Other works (e.g. Meyers & Burchat 2015b; Eriksen & Hoekstra 2018) have shown that the wavelength dependence of the PSF can be corrected for in WL analyses if it is known. Meyers & Burchat (2015b) argue that since a size versus wavelength relation of the form $R \propto \lambda^{-b}$ with $b = 0.2$ leads to a systematic error, if uncorrected, that is roughly $10\times$ greater than the systematic error budget of the LSST WL shear survey, the power-law exponent needs to be known to $\Delta b \sim 0.02$. A similar but even tighter constraint is found in Eriksen & Hoekstra (2018) for *Euclid*. In the previous section, we infer this power-law exponent from the dependence of the PSF size on colour and get physically reasonable values. However, since we do not know the ground truth of the wavelength dependence, we cannot conclude whether the inferred exponent is accurate enough to correct for the PSF chromaticity. To answer this question, we require simulations where the ground truth can be known. In this section, we explore how many stars are needed to determine b to ~ 0.02 . We make a series of postage-stamp images of stars, add noise, and measure the size and flux of these images. We then solve for b in the same way as with the data. While this analysis is applicable to other imaging surveys, we focus on the LSST survey since chromatic biases will be the most significant concern for a survey with the statistical power of LSST.

3.1 Accuracy of the Inferred Wavelength Dependence

We start with a catalogue of stellar SEDs with magnitudes within the range $17 < i < 22$, generated in a 1° radius circle at $(\alpha = 0:0, \delta = 0:0)$ using the CATSIM Milky Way simulator. Stars in this magnitude range will have $S/N \gtrsim 30$ in a single LSST visit while not saturating. The simulator provides estimates of the AB magnitude at 5000 \AA for each star and from this we calculate the expected number of counts in each image using the collecting area of LSST, the exposure time (30 s) for each visit, and the gain (which we take to be $1.7e^-/\text{ADU}$). Poisson noise is added to each pixel in the postage stamp along with noise associated with the sky foreground photons, estimated using the LSST PHOSIM (Peterson et al. 2015).

As we have seen, the atmospheric PSF dominates the chromaticity, and so we include only this component in the simulations. Since we are here focused on the PSF size, we are not interested in the effects of short exposure time (which should affect PSF ellipticity more (e.g. Heymans et al. 2012; Chang et al. 2013)) and we will consider the long-exposure limit PSFs. We assume a von Kármán turbulence power spectrum with an outer scalelength of 10 m (which is on the short side of what is to be expected). The atmospheric PSFs are generated by Fourier transforming the resulting atmospheric structure function (see Appendix A). Atmospheric PSFs are generated at several wavelengths across each band. These monochromatic PSFs are combined with each stellar SED to create the broad-band PSF for each object. The second moments are measured from the postage stamps using the same HSM algorithm as in the HSC data. We also add scatter in the measured size due to errors in the PSF modelling. We consider both the case in which the PSF modelling is perfect and also in which it is accurate to an rms

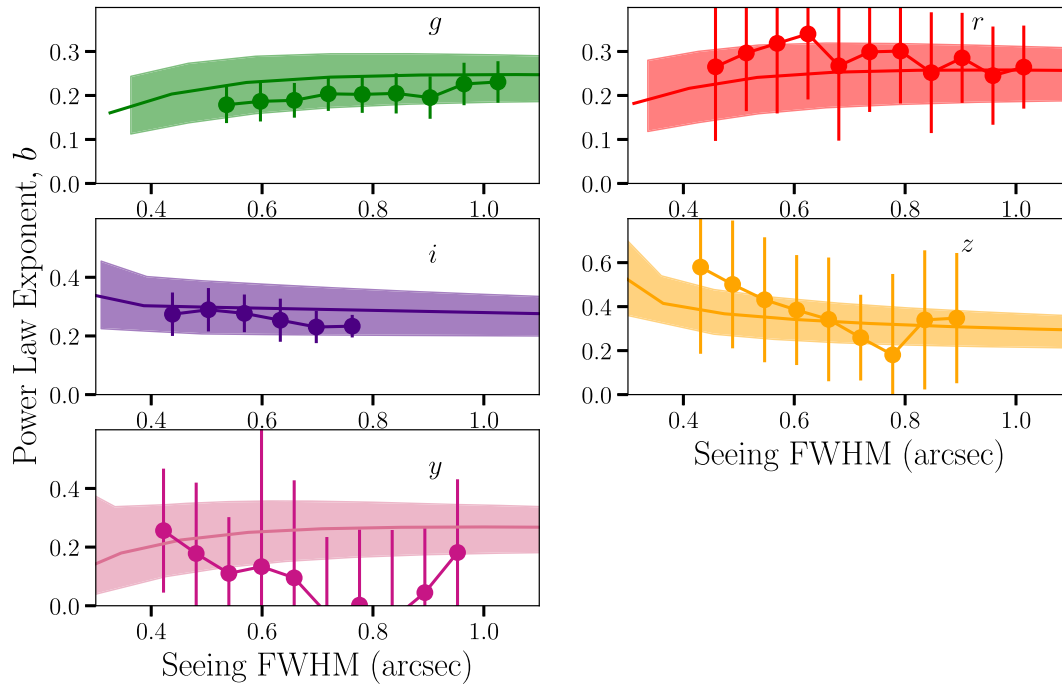


Figure 5. The power-law exponent of the PSF size versus wavelength relation, b , as observed and as modelled. The data points are the data from Fig. 3 smoothed by a running mean of box size 0.1 arcsec. The error bars represent the standard deviation in each bin. The model includes contributions from the atmosphere and the HSC instrument. The coloured region gives the model predictions ranging from an outer scalelength of 8 m (top) and a Kolmogorov atmosphere (bottom) and the inner line is the prediction for an outer scalelength of 25 m. The model does a good job of fitting the trends seen in g , r , i , and, to a lesser extent, z . In y , the diffraction within the CCD seen in Fig. 6 obscures the chromatic effect.

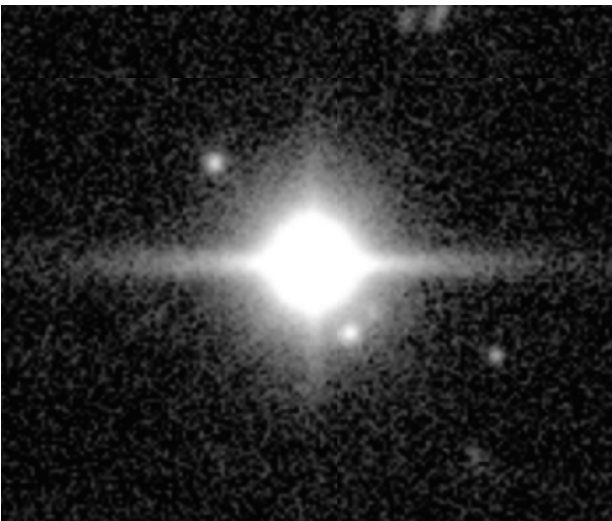


Figure 6. An example of the ‘cross’-shaped pattern around bright sources in the y band due to diffraction within the CCD. The large horizontal spike is parallel to the serial register of the CCD. The star is not saturated and is characteristic of a ~ 19 th mag star in y .

of ± 1 per cent, which is characteristic of the PSF modelling in the HSC survey (Mandelbaum et al. 2018). By fitting a power law to the size of the (noiseless) monochromatic PSFs, we can determine the ‘ground truth’ chromaticity and compare to what we infer from the broad-band images of the stars.

We can check how the accuracy of the inferred chromaticity depends on the number of stars simulated. As in the HSC pipeline, simulated stars are limited to those with more than 12 500 counts

($S/N \gtrsim 60$), which reduces the number of stars by ~ 25 per cent. The measured size of the stars is plotted against the measured colour and the chromaticity is inferred in the same way as in Section 2, using the LSST filter response curves to generate the look-up table. Fig. 7 shows the resulting average of the absolute value of the error in the inferred power-law exponent of the size–wavelength relation (i.e. the parameter b) as a function of the number of $17 < i < 22$ stars used in the simulation. The mean error in the power-law exponent decreases as more stars are simulated, as expected. Considering that 2000–8000 stars were used in each HSC visit in Section 2, the power-law exponents we derived in that section are likely to be accurate to $\Delta b \sim 0.07$ in r , $\Delta b \sim 0.02$ in i and g , and $\Delta b \sim 0.2$ in z , assuming the modelling of the PSF is accurate to 1 per cent rms. These different levels of accuracy are due to a combination of the width of the band, the width of the colour cut used, and the variation in the slope of the stellar SEDs across that band. This trend is consistent with the fact that the r and z bands show more scatter than i and g in the HSC data, as we saw in Fig. 3.

To understand what Fig. 7 means for LSST, it is important to know how many stars are likely to be in each LSST visit. CATSIM predicts $\sim 20\,000$ – $80\,000$ stars with $17 < i < 22$ in the whole $3^\circ 5$ diameter LSST FOV for galactic longitudes between 80° and 40° . These numbers correspond to roughly 0.5 to 2 stars arcmin $^{-2}$. If all these stars are used to determine the PSF–wavelength relation, it would be sufficient to determine b to $\Delta b \sim 0.02$ in at least the g , r , and i bands, even when PSF modelling errors are considered.

3.2 Variations in the Chromaticity with Focal Plane Position

We found evidence for a weak dependence of PSF chromaticity on position in the focal plane of HSC. The same might be true

for the LSST. To consider the optical component of the PSF, we use PHOSIM to simulate the chromaticity at different positions in the focal plane. PHOSIM forces the wavelength dependence of the PSF to have the Kolmogorov $\lambda^{-0.2}$ result, therefore we replace PHOSIM's in-built atmospheric simulation with our own that produces a more realistic wavelength dependence. We generate 500 phase screens in the usual Fourier way (e.g. McGlamery 1976) with a von Kármán power spectrum for the central wavelength in that band. The phase screens are masked with the expected LSST pupil and Fourier transformed to give instantaneous atmospheric PSFs, which are then ensemble-averaged to give a long-exposure atmospheric PSF. Deflection angles are then drawn from this PSF and given to photons as they pass through the atmosphere. The wavelength dependence is included by scaling the deflection angle by a term proportional to the ratio of the PSF size at the photon's wavelength to that at the band's central wavelength. This ratio comes from the numerical fitting of Tokovinin (2002)⁶:

$$\epsilon_{\text{vK}} = \epsilon_{\text{Kolm}} \sqrt{1 - 2.183 \left(\frac{r_0}{L_0} \right)^{0.356}}, \quad (5)$$

where ϵ_{vK} is the PSF FWHM at the desired wavelength, ϵ_{Kolm} is the PSF FWHM for Kolmogorov turbulence ($\propto \lambda^{-0.2}$), r_0 is the usual Fried's parameter ($\propto \lambda^{1.2}$, see Appendix A), and L_0 is the outer scalelength. Tokovinin (2002) finds that equation (5) is accurate to 1 per cent for most values of r_0 and L_0 . This equation has been validated in more recent works (Martinez et al. 2010; Martinez 2014).

By simulating monochromatic sources on multiple chips at different positions in the focal plane, we find that the power-law exponent, b , decreases further from the centre of the FOV (Fig. 8) in the r and z band. In the r band, the instrumental PSF (including both optics and CCD effects) is mostly achromatic and is larger further from the centre of the focal plane and thus dilutes the chromaticity from the atmosphere. The inclusion of charge diffusion in the r band decreases the overall wavelength dependence by increasing the size of the instrumental PSF. In the z band, however, the instrumental PSF from the CCD is highly chromatic and actually reverses the wavelength dependence relative to the atmosphere. As mentioned above and in Meyers & Burchat (2015a), the fast LSST optics and the wavelength-dependent photon absorption length in silicon cause larger PSFs at longer wavelengths that is opposite the atmospheric trend. This effect is more significant further from the centre of the focal plane, causing the power-law exponent, b , to decrease in Fig. 8. In the r and z bands, the changes with position are larger than the accuracy to which the exponent needs to be measured. Thus, PSF chromaticity will have to be measured as a function of focal-plane position. To have $\Delta b \leq 0.02$, the FOV would have to be broken into roughly 0.3 wide annuli in the PSF analysis. Assuming $1 \text{ star arcmin}^{-2}$, this would mean ~ 4000 stars in an annulus about halfway out in the focal plane. This number of stars is small enough

⁶This scaling implicitly assumes that the wavelength dependence is simply a dilation/contraction of the PSF. This is strictly true for the Kolmogorov PSF but is not true for the von Kármán PSFs. For the latter, redder wavelengths have smaller PSFs but their wings become more pronounced, causing the trace radius to fall more slowly with wavelength than the FWHM. Therefore, using equation (5) will overestimate the chromaticity by 5–10 per cent in the parameter b , thus the b values in Fig. 8 are higher than they likely will ever be for LSST. For the purpose of this simulation, this is irrelevant since we are not focused on the absolute level of chromaticity but on how the chromaticity changes with position in the focal plane.

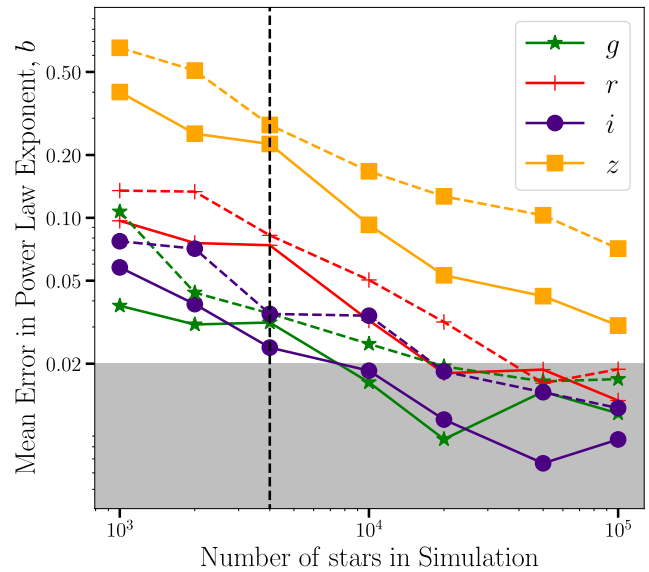


Figure 7. The average of the absolute value of the error in the determination in the power-law exponent of the PSF size–wavelength relation as a function of the number of $17 < i < 22$ stars used in the simulation. The final number of stars used in the analysis is somewhat less due to the flux and colour cuts, as described in the text. The dashed lines are for the case where there is 1 per cent rms error in the modelling of the PSF and the solid lines are for perfect PSF modelling. An outer scalelength of 10 m is assumed for the atmosphere. The ‘ground truth’ wavelength dependence for the simulations is $R \propto \lambda^{-0.31}$ for g , $R \propto \lambda^{-0.33}$ for r , $R \propto \lambda^{-0.35}$ for i , and $R \propto \lambda^{-0.36}$ for z . The grey area denotes the goal of $\Delta b \leq 0.02$. The vertical black dashed line represents $1 \text{ star arcmin}^{-2}$ for a 0.3 wide annulus at half the radius of the LSST focal plane (see the text). The average error goes down as roughly $N_{\text{stars}}^{-0.5}$.

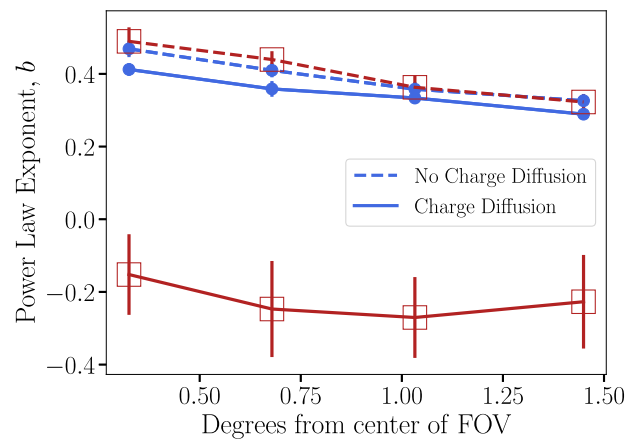


Figure 8. The measured (negative) power-law exponent of the size versus wavelength relation, i.e. b , in the r band (blue circles) and z band (red squares) as a function of LSST focal-plane position in PHOSIM. An outer scalelength of 10 m and Fried's parameter, r_0 , of 10 cm is used, representing the worst-case atmospheric wavelength dependence that the LSST could expect. The dashed lines do not include charge diffusion or other chromatic effects in the CCDs, while the solid lines do.

that it will only be possible to determine the power-law exponent to a mean error of $\Delta b \sim 0.03$ in i , allowing one to correct most, but not all, of the chromatic bias (Fig. 7). In r band it will only be possible to determine the power-law exponent to $\Delta b \sim 0.07$ if the PSF modelling errors are included.

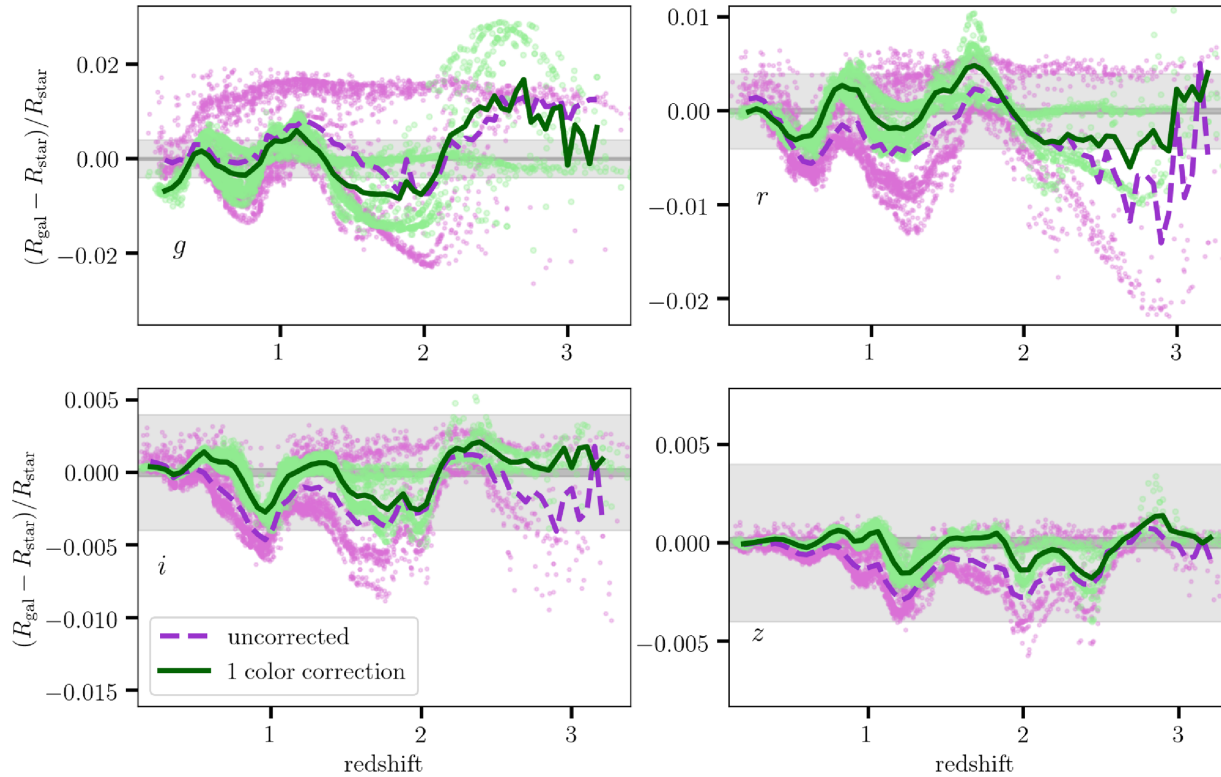


Figure 9. The relative difference between the PSF size for a series of galactic SEDs and that of a K5V star SED as a function of galaxy redshift. The purple points assume no chromatic correction to the PSF, while the green points include a single colour correction assuming that $b = -0.45$ (and is determined to $\Delta b \sim 0.02$). The light grey band shows the HSC SSP first-year WL error budget of 0.004 and the dark grey band shows that of the LSST survey of 2.7×10^{-4} . The lines show a running mean of the points.

However, if a physical model of the optics can be constructed such that the instrumental PSF and detector chromaticity can be modelled throughout the focal plane, then all the stars in a visit can be used to infer the atmospheric chromaticity. This would allow for a very accurate determination of the atmospheric parameters. Such a model is planned as part of the PSF modelling in LSST. Additionally, while there is some evidence that the atmospheric outer scalelength changes with time within a night (Linfield et al. 2001), it likely does not change significantly between exposures. Thus, stars detected in a few adjacent exposures can be used to constrain the atmospheric parameters. In the HSC data, we find that the power-law exponent, b , can change on the level of $\Delta b \sim 0.1$ on the scale of an hour and on the level of $\Delta b \sim 0.3$ over the course of a night.

4 DISCUSSION AND SUMMARY

In this paper, we explored the wavelength dependence of PSFs present in a modern, optical imaging survey. We find that redder sources have significantly smaller PSFs than blue sources in the HSC SSP survey data. This effect is at the ~ 1 per cent level for the g , r , and i bands and about an order of magnitude smaller for z and y . We infer that the monochromatic PSF size follows a power law with wavelength of the form $\propto \lambda^{-0.2}$ to $\propto \lambda^{-0.5}$ depending on the exposure. We argue that this is consistent with the expectations of a turbulent atmosphere whose turbulent power spectrum saturates at an outer scalelength of ~ 10 m– 100 m. We find some evidence that the level

of wavelength dependence is reduced in the g and r bands when the atmospheric seeing is very good, because the optical/instrumental PSF in these bands is roughly achromatic. The opposite effect occurs in the z band because charge diffusion in the CCD, which dominates in good seeing, has an even steeper wavelength dependence than the atmosphere. The i band is intermediate; the optical/instrumental PSF has roughly the same level of chromaticity as the atmospheric PSF. The analysis of y band is complicated by the fact that silicon is practically transparent to photons on the redward edge of y , causing photons to be absorbed after they bounce off the bottom of the silicon. This leads to large spikes present in the HSC- y images.

Since most of the PSF chromaticity comes from the atmosphere, upcoming ground-based projects like the LSST will suffer from the same effects. Meyers & Burchat (2015b) showed that a PSF wavelength dependence of $\lambda^{-0.2}$, if unmodelled, would interfere with WL science since galaxies will have smaller effective PSFs than the bulk of the stars used to model the PSF. If left uncorrected, the shear will be overestimated and cosmological parameters will be biased. In Fig. 9, we show the difference between the PSF size for a variety of galactic SEDs relative to that of a K5V star assuming a monochromatic wavelength dependence of $\lambda^{-0.45}$, typical of the worst cases we found in r and i in the HSC data. Since a K5V star has an intermediate colour, it should be roughly representative of the PSF modelling (which is based on stars of a range of colour) when no chromatic effects are included. The galactic SEDs come from the LSST CATSIM project. CATSIM starts with the

simulated galaxy catalogue of De Lucia et al. (2006) and attaches an SED to each galaxy based on the stellar population models of Bruzual & Charlot (2003). We plot 4000 galaxies with $i < 25$. Meyers & Burchat (2015b) give the LSST PSF size modelling requirement as $|\langle \Delta R^2/R^2 \rangle| < 5.5 \times 10^{-4}$, corresponding to $|\langle \Delta R/R \rangle| < 2.7 \times 10^{-4}$, the quantity we constrain in this paper. We also show the first year HSC WL science requirement of $|\langle \Delta R/R \rangle| \lesssim 0.004$ described in Mandelbaum et al. (2018). The average PSF error size is clearly well above the error budget for LSST and will have to be corrected for in the PSF modelling. We also show a rough correction algorithm using a single colour. 2000 separate galactic SEDs drawn from the same distribution are used to derive a linear relation between the PSF size error and the SED colour, assuming that the PSF size–wavelength relation is incorrect by $\Delta b \sim 0.02$ (in other words, we use $\text{size} \propto \lambda^{-0.43}$ to account for errors in measuring this relation). For the g band we use $g - r$ colour, for r and i we use $r - i$, and for z we use $i - z$. This relation is used to scale the band-averaged PSF used for galaxies based on their colour so that they match the fiducial stellar PSF. As can be seen in Fig. 9, this correction removes a redshift-independent offset in the r , i , and z bands but leaves significant redshift-dependent structure.

This quick demonstration shows that a more complicated algorithm that makes use of photometry in all five or six bands available is required, like the algorithms described in Meyers & Burchat (2015b) and Eriksen & Hoekstra (2018). These previous works showed that, if the wavelength dependence of the PSF is known to $\Delta b \sim 0.02$, the chromatic bias can be corrected for to the requirements of the LSST and *Euclid*. In this work, we have shown that the wavelength dependence varies significantly with time due to the atmosphere but can be measured very accurately from the stars in the image frames. This work also highlights the need for a physical model of the LSST optical PSF so that all the stars across the focal plane can be used to constrain the atmospheric parameters. Such a model will also be necessary when using the measured wavelength dependence to generate ‘per-object’ PSFs given a source SED, but that is beyond the scope of the current work.

ACKNOWLEDGEMENTS

We thank Rachel Mandelbaum for useful comments on this manuscript and Jim Gunn for enlightening discussions. We also thank the anonymous referee for insightful comments that significantly improved the paper.

The HSC collaboration includes the astronomical communities of Japan and Taiwan, and Princeton University. The HSC instrumentation and software were developed by the National Astronomical Observatory of Japan (NAOJ), the Kavli Institute for the Physics and Mathematics of the Universe (Kavli IPMU), the University of Tokyo, the High Energy Accelerator Research Organization (KEK), the Academia Sinica Institute for Astronomy and Astrophysics in Taiwan (ASIAA), and Princeton University. Funding was contributed by the FIRST program from Japanese Cabinet Office, the Ministry of Education, Culture, Sports, Science and Technology (MEXT), the Japan Society for the Promotion of Science (JSPS), Japan Science and Technology Agency (JST), the Toray Science Foundation, NAOJ, Kavli IPMU, KEK, ASIAA, and Princeton University.

The Pan-STARRS1 Surveys (PS1) (Schlafly et al. 2012; Tonry et al. 2012; Magnier et al. 2013) have been made possible through contributions of the Institute for Astronomy, the University of

Hawaii, the Pan-STARRS Project Office, the Max-Planck Society and its participating institutes, the Max Planck Institute for Astronomy, Heidelberg and the Max Planck Institute for Extraterrestrial Physics, Garching, The Johns Hopkins University, Durham University, the University of Edinburgh, Queen’s University Belfast, the Harvard-Smithsonian Center for Astrophysics, the Las Cumbres Observatory Global Telescope Network Incorporated, the National Central University of Taiwan, the Space Telescope Science Institute, the National Aeronautics and Space Administration under Grant No. NNX08AR22G issued through the Planetary Science Division of the NASA Science Mission Directorate, the National Science Foundation under Grant No. AST-1238877, the University of Maryland, and Eotvos Lorand University (ELTE).

This paper makes use of software developed for the LSST. We thank the LSST Project for making their code available as free software at <http://dm.lsst.org>.

Based in part on data collected at the Subaru Telescope and retrieved from the HSC data archive system, which is operated by the Subaru Telescope and Astronomy Data Center at National Astronomical Observatory of Japan.

REFERENCES

- Aihara H. et al., 2018a, *PASJ*, 70, S4
 Aihara H. et al., 2018b, *PASJ*, 70, S8
 Alejandro Plazas A., Bernstein G., 2012, *PASP*, 124, 1113
 Amara A., Réfrégier A., 2008, *MNRAS*, 391, 228
 Antilogus P., Astier P., Doherty P., Guyonnet A., Regnault N., 2014, *J. Instrum.*, 9, C03048
 Axelrod T., Kantor J., Lupton R. H., Pierfederici F., 2010, *Proc. SPIE*, 7740, 10.
 Baraffe I., Homeier D., Allard F., Chabrier G., 2015, *A&A*, 577, A42
 Bertin E., 2013, *PSFEX: Point Spread Function Extractor*, Astrophysics Source Code Library, ascl:1301.001
 Bosch J. et al., 2018, *PASJ*, 70, S5
 Bruzual G., Charlot S., 2003, *MNRAS*, 344, 1000
 Chang C. et al., 2013, *MNRAS*, 428, 2695
 Conan R., 2008, *J. Opt. Soc. Am. A*, 25, 526
 Conan R., Ziad A., Borgnino J., Martin F., Tokovinin A. A., 2000, in Léna P., Quirrenbach A., eds, *Proc. SPIE Conf. Ser. Vol. 4006, Interferometry in Optical Astronomy*. SPIE, Bellingham, p. 963
 Coulman C. E., Vernin J., Coqueugniot Y., Caccia J.-L., 1988, *Appl Opt.*, 27, 155
 Coulton W. R., Armstrong R., Smith K. M., Lupton R. H., Spergel D. N., 2017, *AJ*, 155, 258
 Covey K. R. et al., 2007, *AJ*, 134, 2398
 Cypriano E. S., Amara A., Voigt L. M., Bridle S. L., Abdalla F. B., Réfrégier A., Seiffert M., Rhodes J., 2010, *MNRAS*, 405, 494
 De Lucia G., Springel V., White S. D. M., Croton D., Kauffmann G., 2006, *MNRAS*, 366, 499
 Eriksen M., Hoekstra H., 2018, *MNRAS*, 477, 3433
 Furusawa H. et al., 2018, *PASJ*, 70, S3
 Heymans C., Rowe B., Hoekstra H., Miller L., Erben T., Kitching T., van Waerbeke L., 2012, *MNRAS*, 421, 381
 Hirata C., Seljak U., 2003, *MNRAS*, 343, 459
 Hufnagel R. E., Stanley N. R., 1964, *J. Opt. Soc. Am.*, 54, 52
 Huterer D., Takada M., Bernstein G., Jain B., 2006, *MNRAS*, 366, 101
 Ivezić Ž. et al., 2008, *ApJ*, 684, 287
 Jee M. J., Tyson J. A., 2011, *PASP*, 123, 596
 Jurić M. et al., 2008, *ApJ*, 673, 864
 Jurić M. et al., 2015, preprint ([arXiv:1512.07914](https://arxiv.org/abs/1512.07914))
 Komiyama Y. et al., 2018, *PASJ*, 70, S2
 Kurucz R., 1993, *SYNTHES Spectrum Synthesis Programs and Line Data*. Smithsonian Astrophys. Obs., Cambridge, p. 13
 Laureijs R. et al., 2011, preprint ([arXiv:1110.3193](https://arxiv.org/abs/1110.3193))

- Léna P., Rouan D., Lebrun F., Mignard F., Pelat D., 2012, *Observational Astrophysics*. Springer-Verlag, Berlin
- Linfield R. P., Colavita M. M., Lane B. F., 2001, *ApJ*, 554, 505
- LSST Science Collaboration et al., 2009, preprint (arXiv:0912.0201)
- Lupton R., Gunn J. E., Ivezić Z., Knapp G. R., Kent S., 2001, in Harnden F. R., Jr, Primiini F. A., Payne H. E., eds, *ASP Conf. Ser. Vol. 238, Astronomical Data Analysis Software and Systems X*. Astron. Soc. Pac., San Francisco, p. 269
- Magnier E. A. et al., 2013, *ApJS*, 205, 20
- Mandelbaum R. et al., 2018, *PASJ*, 70, S25
- Mandelbaum R., 2017, preprint (arXiv:1710.03235)
- Martinez P., 2014, *A&A*, 572, A14
- Martinez P., Kolb J., Sarazin M., Tokovinin A., 2010, *The Messenger*, 141, 5
- Massey R. et al., 2013, *MNRAS*, 429, 661
- McGlamery B. L., 1976, in Urbach J. C., ed., *Proc SPIE Vol. 74, Image Processing*. SPIE, Bellingham, p. 225
- McKechnie T. S., 2016, *General Theory of Light Propagation and Imaging Through the Atmosphere*. Springer, Cham
- Meyers J. E., Burchat P. R., 2015a, *J. Instrum.*, 10, C06004
- Meyers J. E., Burchat P. R., 2015b, *ApJ*, 807, 182
- Miyazaki S. et al., 2018, *PASJ*, 70, S1
- Ono Y. H., Correia C. M., Andersen D. R., Lardiére O., Oya S., Akiyama M., Jackson K., Bradley C., 2017, *MNRAS*, 465, 4931
- Oya S., Terada H., Hayano Y., Watanabe M., Hattori M., Minowa Y., 2016, *Experimental Astronomy*, 42, 85
- Paulin-Henriksson S., Amara A., Voigt L., Refregier A., Bridle S. L., 2008, *A&A*, 484, 67
- Peterson J. R. et al., 2015, *APJS*, 218, 14
- Pickles A. J., 1998, *PASP*, 110, 863
- Roddirer F., 1981, *Progress in Optics*. Volume 19. North-Holland Publishing Co., Amsterdam, p. 281
- Rowe B. T. P. et al., 2015, *Astron. Comput.*, 10, 121
- Schlafly E. F. et al., 2012, *ApJ*, 756, 158
- Semboloni E. et al., 2013, *MNRAS*, 432, 2385
- Tokovinin A., 2002, *PASP*, 114, 1156
- Tokovinin A., Sarazin M., Smette A., 2007, *MNRAS*, 378, 701
- Tonry J. L. et al., 2012, *ApJ*, 750, 99
- Voigt L. M., Bridle S. L., Amara A., Cropper M., Kitching T. D., Massey R., Rhodes J., Schrabback T., 2012, *MNRAS*, 421, 1385
- von Kármán T., 1948, *Proc. Natl. Acad. Sci. USA*, 34, 530
- Xin B., Ivezić Z., Lupton R. H., Peterson J. R., Yoachim P., Jones R. L., Claver C. F., Angeli G., 2018, preprint (arXiv:1805.02845)
- Ziad A., Conan R., Tokovinin A., Martin F., Borgnino J., 2000, *Appl. Opt.*, 39, 5415
- Connolly A. J., Angeli G. Z., Chandrasekharan S., Claver C. F., Cook K., Ivezić Z., Jones R. L., Krughoff K. S., Peng E. H., Peterson J., Petry C., Rasmussen A. P., Ridgway S. T., Saha A., Sembroski G., vanderPlas J., Yoachim P., 2014, *Modeling, Systems Engineering, and Project Management For Astronomy VI*, 9150:14

APPENDIX A: ATMOSPHERIC CHROMATICITY WITH AN OUTER SCALE

A1 Long Exposure PSF Profile

We present a brief review of atmospheric turbulence theory in the atmosphere as it applies to observed PSFs. We include results from Roddirer (1981), McKechnie (2016), and Léna et al. (2012).

From the Fraunhofer diffraction equation, the observed PSF (ignoring non-diffraction-limited optical effects) is the squared modulus of the Fourier transform of the complex amplitude of the electric field at the pupil plane. We are interested in the PSF of long exposure images ($\gtrsim 30$ sec, which is the exposure time for the LSST survey) and so we will consider a time average over the atmospheric turbulence. Assuming that the processes are ergodic, this is equivalent to

a spatial average. Therefore, to predict the intensity profiles in the observed image, we need to know the spatial coherence function of the complex amplitude of the electric field of a wave, $\Psi(\vec{x})$, after it goes through a thin turbulent layer. We will later integrate over all layers. The coherence function is defined as:

$$B_{\Psi}(\vec{\zeta}) \equiv \langle \Psi(\vec{x})\Psi^*(\vec{x} + \vec{\zeta}) \rangle, \quad (\text{A1})$$

where \vec{x} is a (2-D) position on the pupil plane. For simplicity, we assume a monochromatic plane wave. Our goal is to connect this function to the power spectrum of index of refraction variations that are causing the phase shifts and thus the blurring. We will assume that the layer is thin enough that it only introduces a phase shift to the field. This means we can write:

$$\Psi = e^{i\phi}, \quad (\text{A2})$$

since we can write $\Psi_{\infty} = 1$ for the wave above the atmosphere, and the coherence function becomes

$$B_{\Psi}(\vec{\zeta}) \equiv \langle e^{i(\phi(\vec{x}) - \phi(\vec{x} + \vec{\zeta}))} \rangle. \quad (\text{A3})$$

The phase, ϕ , should be the sum of a large number of independent perturbations (as long as the thickness of the layer is greater than the outer scale of turbulence) and therefore should be Gaussian randomly distributed (due to the central limit theorem). We can then use a simple identity for the Gaussian distributed variable to write:

$$\begin{aligned} B_{\Psi}(\vec{\zeta}) &= \exp \left[-\frac{1}{2} \langle |\phi(\vec{x}) - \phi(\vec{x} + \vec{\zeta})|^2 \rangle \right] \\ &\equiv \exp \left[-\frac{1}{2} D_{\phi}(\vec{\zeta}) \right] \end{aligned} \quad (\text{A4})$$

which defines the phase structure function, D_{ϕ} . The goal is now to find the phase structure function in terms of the index of refraction variations which are causing the phase perturbations. We start with the coherence function of the phase, ϕ :

$$B_{\phi}(\vec{\zeta}) \equiv \langle \phi(\vec{x})\phi(\vec{x} + \vec{\zeta}) \rangle \quad (\text{A5})$$

From this definition, it is easy to show that

$$D_{\phi}(\vec{\zeta}) = 2 \left[B_{\phi}(0) - B_{\phi}(\vec{\zeta}) \right] \quad (\text{A6})$$

The phase perturbation that a layer of thickness δh causes is simply:

$$\phi(\vec{x}) = k \int_h^{h+\delta h} n(\vec{x}, z) dz \quad (\text{A7})$$

where k is the wavenumber, and n is the index of refraction. Plugging this into equation A5 we find:

$$\begin{aligned} B_{\phi}(\vec{\zeta}) &= k^2 \int_h^{h+\delta h} \int_h^{h+\delta h} dz dz' \langle n(\vec{x}, z)n(\vec{x} + \vec{\zeta}, z') \rangle \\ &= 2k^2 \int_h^{h+\delta h} dz \int_z^{h+\delta h} dz' \langle n(\vec{x}, z)n(\vec{x} + \vec{\zeta}, z') \rangle \end{aligned} \quad (\text{A8})$$

where we have used the fact that the term in the angle brackets is symmetric to exchanging z and z' . Defining $\xi \equiv z' - z$ and B_n as the 3-dimensional covariance function of n , we can switch the order of integration and, assuming that n varies slowly with z (Hufnagel & Stanley 1964; McKechnie 2016), we find:

$$B_{\phi}(\vec{\zeta}) = 2k^2 \int_0^{\delta h} d\xi \int_h^{h+\delta h-\xi} dz B_n(\vec{\zeta}, \xi) \quad (\text{A9})$$

We've assumed above that the thickness of the layer, δh , is larger than the outer scale of turbulence, so $B_n \rightarrow 0$ for $\xi > \delta h$ and we can replace the ξ integral upper bound with ∞ . Because B_n is roughly

independent of z , we can take B_n out of the z integral, leaving $\delta h - \xi$. Since $B_n \approx 0$ unless $\xi < \delta h$, we can approximate $\delta h - \xi \approx \delta h$. Also since B_n is symmetric with respect to ξ , we can extend the bottom bound to $-\infty$ and absorb the factor of 2:

$$B_\phi(\vec{\zeta}) = k^2 \delta h \int_{-\infty}^{+\infty} d\xi B_n(\vec{\zeta}, \xi) \quad (\text{A10})$$

In general, the two-point covariance function is the Fourier transform of the power spectrum of the field:

$$\Phi(\vec{f}) = \int d\vec{\zeta} B(\vec{\zeta}) e^{-2\pi i \vec{f} \cdot \vec{\zeta}} \quad (\text{A11})$$

Using equation A10 in A11 we can relate the 2D phase power spectrum, Φ_ϕ , to the 3D power spectrum of index of refraction fluctuations, Φ_n .

$$\begin{aligned} \Phi_\phi(\vec{f}) &= \int d\vec{\zeta} k^2 \delta h \int d\xi B_n(\vec{\zeta}, \xi) e^{-2\pi i \vec{f} \cdot \vec{\zeta}} \\ &= k^2 \delta h \Phi_n(\vec{f}, 0) \end{aligned} \quad (\text{A12})$$

Following Conan (2008), we use the von Kármán (1948) power spectrum for the index of refraction variations:

$$\Phi_n(\vec{f}, 0) = 0.0097 C_n^2 (f^2 + f_0^2)^{-11/6} \quad (\text{A13})$$

where C_n is the index of refraction *structure constant*, $f \equiv |\vec{f}|$, and $f_0 \equiv 1/L_0$ is the inverse of the outer scale of turbulence. This means that the power spectrum saturates on scales larger than L_0 . f is a spatial frequency with units $[m^{-1}]$.

Finally, we use this power spectrum to calculate $D_\phi(\vec{\zeta})$. From equation (A12), the phase power spectrum is

$$\Phi_\phi(\vec{f}) = 0.0097 k^2 \delta h C_n^2 (f^2 + f_0^2)^{-11/6}, \quad (\text{A14})$$

and the phase covariance function is the inverse FT of this:

$$B_\phi(\vec{\zeta}) = 0.036 k^2 \delta h C_n^2 f_0^{-5/3} (2\pi \zeta f_0)^{5/6} K_{5/6}(2\pi f_0 \zeta), \quad (\text{A15})$$

where $K_\nu(x)$ is the modified Bessel function of the second kind of order ν . The numerical constants come from various gamma functions that come from integrating equation (A14). This result is the output from one single layer, but we can combine the effect of several atmospheric layers by integration over height:

$$\begin{aligned} B_\phi(\vec{\zeta}) &= 0.036 k^2 f_0^{-5/3} (2\pi \zeta f_0)^{5/6} K_{5/6}(2\pi f_0 \zeta) \int dz C_n^2(z) \\ &= 0.036 k^2 f_0^{-5/3} (2\pi \zeta f_0)^{5/6} K_{5/6}(2\pi f_0 \zeta) \sigma^2 \end{aligned} \quad (\text{A16})$$

where $\sigma^2 \equiv \int dz C_n^2(z)$, with units of $[m^{-1/3}]$. This quantity is related to Fried's parameter as $r_0 = 0.1846(\lambda/\sigma)^{6/5}$. Also note that the above step implicitly assumes that the outer scalelength does not change with altitude.

We can now use this in equation (A6) to write:

$$\begin{aligned} D_\phi(\vec{\zeta}) &= 2 \left[0.036 f_0^{-5/3} \frac{\Gamma(5/6)}{2^{1/6}} k^2 \sigma^2 \right. \\ &\quad \left. - 0.036 k^2 f_0^{-5/3} (2\pi \zeta f_0)^{5/6} K_{5/6}(2\pi f_0 \zeta) \sigma^2 \right] \\ &= 0.072 \left(\frac{2\pi \sigma}{\lambda} \right)^2 f_0^{-5/3} \left[\frac{\Gamma(5/6)}{2^{1/6}} \right. \\ &\quad \left. - (2\pi f_0 \zeta)^{5/6} K_{5/6}(2\pi f_0 \zeta) \right] \end{aligned} \quad (\text{A17})$$

where we have used $k = 2\pi/\lambda$.

By taking equation A17 to the limit of $f_0 \rightarrow 0$ and using Fried's parameter, we get the phase structure function for Kolmogorov turbulence:

$$D_\phi^{\text{Kolm}}(\zeta) = 6.88 \left(\frac{\zeta}{r_0} \right)^{5/3} \quad (\text{A18})$$

With (either) structure function in hand, we can calculate the wavefront's covariance function via equation A4. Note that we calculated equation A4 for the wave right after it leaves the layer. It is shown in Roddier (1981) and Léna et al. (2012) that this coherence function does not change due to Fresnel diffraction through the atmosphere from this thin layer to the ground layer (it only picks up an overall phase) and so the coherence function at the telescope's pupil plane is:

$$B_{\psi,0}(\zeta) = B_\psi(\zeta) = \exp \left[-\frac{1}{2} D_\phi(\vec{\zeta}) \right] \quad (\text{A19})$$

We can now simply write out the expected image in the image plane, assuming isotropy of turbulence and ignoring the modulus transfer function of the telescope (McKechnie 2016), as:

$$\langle I(\theta) \rangle = \int_{\text{aperture}} B_\psi(\zeta) \zeta J_0 \left(\frac{2\pi \zeta \theta}{\lambda} \right) d\zeta \quad (\text{A20})$$

We use equation (A20) to generate the model atmospheric PSFs in Sections 2 and 3.

A2 Wavelength Dependence

We mention in the introduction that a finite outer scalelength steepens the wavelength dependence of this PSF. To see the wavelength dependence of the PSF, we can consider a structure function of the general form

$$D_\phi(\zeta) = 2\beta \zeta^\alpha, \quad (\text{A21})$$

Using equation A20 and the fact that the integral loses support for large ζ , it is possible to show that the FWHM of this PSF is roughly given by

$$\theta_{\text{FWHM}} \approx \frac{\lambda}{\pi} \sqrt{\frac{4\Gamma\left(\frac{2+\alpha}{\alpha}\right)}{\Gamma\left(\frac{4+\alpha}{\alpha}\right)}} \beta^{1/\alpha}, \quad (\text{A22})$$

If we consider the structure function for Kolmogorov turbulence (equation A18), $\beta \sim \lambda^{-2}$ and $\alpha = 5/3$ so

$$\theta_{\text{FWHM}} \sim \lambda^{-1/5} \quad (\text{A23})$$

which is the familiar result. A more accurate numerical calculation gives the FWHM in Kolmogorov turbulence as (Tokovinin 2002):

$$\theta_{\text{FWHM, Kolm}} = 0.98 \frac{\lambda}{r_0} \quad (\text{A24})$$

where $r_0 \propto \lambda^{6/5}$.

It is not easy to analytically show the wavelength dependence in the case of the more general von Kármán turbulence. Instead, we do the Fourier transform in equation (A20) numerically and measure the FWHM directly from the resulting profile. The results are shown in Fig. A1, where it is seen that the smaller the outer scalelength, the steeper the wavelength dependence of the FWHM. Additionally,

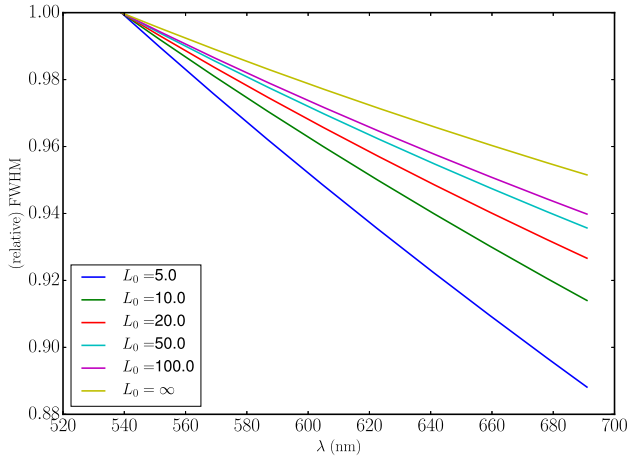


Figure A1. Relative FWHM of the atmospheric PSF as a function of wavelength in the r -band for different outer scalelengths in meters. The FWHM increases as one increases the outer scalelength at a fixed wavelength.

a very short outer scalelength causes the wavelength dependence of the PSF to deviate from a power law and become more linear. However, for outer scalelengths $\gtrsim 10\text{m}$ which is what is expected for common observatory sites, the power law approximation we made in Section 2 is accurate.

This paper has been typeset from a $\text{\TeX}/\text{\LaTeX}$ file prepared by the author.